ORNL/TM-2022/2668

Microstructural Characterization of the Second High Fluence Baffle-Former Bolt Retrieved from a Westinghouse Two-loop Downflow Type PWR

Timothy G. Lach
Xiang (Frank) Chen
Thomas M. Rosseel

September 2022

OAK RIDGE National Laboratory

ORNL IS MANAGED BY UT-BATTELLE LLC FOR THE US DEPARTMENT OF ENERGY

ORNL/TM-2022/2668

Light Water Reactor Sustainability (LWRS) Program
M3LW-22OR0402053

MICROSTRUCTURAL CHARACTERIZATIONS OF THE SECOND HIGH FLUENCE BAFFLE-FORMER BOLT RETRIEVED FROM A WESTINGHOUSE TWO-LOOP DOWNFLOW TYPE PWR

Timothy G. Lach, Xiang (Frank) Chen, Thomas M. Rosseel

Materials Science and Technology Division
Oak Ridge National Laboratory

September 2022

Prepared by
OAK RIDGE NATIONAL LABORATORY
Oak Ridge, TN 37831-6136
managed by
UT-BATTELLE LLC
for the
US DEPARTMENT OF ENERGY
under contract DE-AC05-00OR22725

This page intentionally left blank

CONTENTS

LIST OF FIGURES

LIST OF TABLES

This page intentionally left blank

ACKNOWLEDGEMENTS

This research was sponsored by the U.S. Department of Energy, Office of Nuclear Energy, Light Water Reactor Sustainability Program, Materials Research Pathway, under contract DE-AC05-00OR22725 with UT-Battelle, LLC/Oak Ridge National Laboratory (ORNL).

Atom probe tomography (APT) research was conducted as part of a user project at the Center for Nanophase Materials Sciences (CNMS), which is a US Department of Energy, Office of Science User Facility at Oak Ridge National Laboratory. We would like to thank Jonathan Poplawsky and James Burns for help with APT data collection

The authors extend their appreciation to Clay Morris, Jerid Metcalf, Mark Delph, and other colleagues at Irradiated Materials Examination and Testing Facility (IMET) at ORNL for their support during sample processing in the hot cell sample retrieval. In addition, we would like to thank Patricia Tedder at the Low Activation Materials Development and Analysis (LAMDA) Laboratory at ORNL for receiving, cleaning, and inventorying the irradiated samples. The authors are grateful to Dr. TS Byun and Dr. Stephen Taller from ORNL for their technical review of this report. We acknowledge Heather Malikowski and Robert Marcello of Exelon Corporation and Bernard Rudell formerly of Exelon Corporation for their assistance during the bolt harvesting process. Lastly, we would like to thank the late Mike Burke formerly with Electrical Power Research Institute who was involved in the bolt havesting and characterization planning and led the sample preparation, machining, and shipping when he was working at Westinghouse Electric Company.

This page intentionally left blank

EXECUTIVE SUMMARY

As one of the pressurized water reactor (PWR) internal components, baffle-former bolts (BFBs) are subjected to significant mechanical stress and neutron irradiation from the reactor core during the plant operation. Over the long operation period, these conditions lead to potential degradation and reduced load-carrying capacity of the bolts. In support of evaluating long-term operational performance of materials used in core internal components, the Oak Ridge National Laboratory (ORNL), through the Department of Energy (DOE), Light Water Reactor Sustainability (LWRS) Program, Materials Research Pathway (MRP) has harvested two high fluence BFBs from a commercial Westinghouse two-loop downflow type PWR. The two bolts of interest, i.e. bolts # 4412 and 4416, were withdrawn from service in 2011 as part of a preventative replacement plan. No identification of cracking or potential damage was found for these bolts during their removal in 2011. However, the bolts required a lower torque for removal from the baffle structure than the original torque specified during installation. Irradiation displacement damage levels in the bolts range from 15 to 41 displacements per atom. The goal of this project is to perform detailed microstructural and mechanical property characterization of BFBs following in-service exposures. The information from these bolts will be integral to the LWRS program initiatives in evaluating end of life microstructure and properties. Furthermore, valuable data will be obtained that can be incorporated into model predictions of long-term irradiation behavior and compared to results obtained in high flux experimental reactor conditions.

In this report, we present our latest study in FY22 on microstructural characterizations of the second high fluence baffle-former bolt, i.e., bolt # 4412. Analytical electron microscopy and atom probe tomography characterization were performed. The radiation-induced defects in the material add to the large wealth of knowledge for neutron-induced defects in 304/316 grades of stainless steels, specifically for radiation-induced precipitation after high fluence commercial PWR irradiation. The main findings are summarized as follows:

1) The cavity size was considerably larger in the bolt thread section than in the bolt head, with the bolt thread section having a bimodal distribution of cavities greater than ~6 nm in diameter and less than ~3 nm in diameter. The bolt head only had the small-sized cavities. In addition, there was a denuded zone of large cavities near grain boundaries in the thread section of the bolt.
2) Radiation-induced precipitation in the BFB #4412 was highly complex, with the volume fraction, size, and number density of Ni/Si and Cu-rich precipitates depending strongly on the radiation temperature/dose. In many cases, co-precipitates of adjoined clusters were found with Ni/Si-rich precipitates sandwiched between Cu-rich clusters and Mo/Cr/P-rich clusters.
3) Solute segregation out of solution was highest for most solutes in the thread section of the bolt #4412 with the exception of Cu, which experienced more separation out of solution into Cu-rich clusters in the bolt head section. This highlights the difference in the mechanisms for precipitation of Ni/Si clusters, which have the Ni_3Si phase composition, and precipitation of Cu-rich clusters.
4) There appear to be multiple simultaneous influences that affect the microstructural variation along the length of the bolt that overcomes the ~2X difference in irradiation dose between the bolt head and the bolt thread. The irradiation temperature, thermal/fast neutron ratio variation, potential strain gradient, and exposure to PWR coolant water that each section of the bolt sees may have more influence on the microstructural evolution than the total irradiation dose. The bolt thread and shank, with higher temperature, higher relative fast neutron flux, higher strain, and exposure to coolant but lower dose, underwent more enhanced cavity formation, precipitation, and solute segregation than the bolt head section.

This page intentionally left blank

1. INTRODUCTION

As one of the pressurized water reactor (PWR) internal components, baffle-former bolts (BFBs) are subjected to significant mechanical stress and neutron irradiation from the reactor core during the plant operation. Over the long operation period, these conditions lead to potential degradation and reduced load-carrying capacity of the bolts, and life extension of existing PWRs would only cause more damage to the bolt material. Indeed, the BFB has been a particular concern for the nuclear industry since the first observation of failed bolts following the investigation of flow-induced vibration of fuel rods in elements on the core periphery observed in French 900 MW plants in the 1980s [1]. In the United States, the first degraded BFBs were observed in 1999. In support of evaluating long-term operational performance of materials used in core internal components, the Materials Research Pathway (MRP) under the U.S. Department of Energy (DOE) Light Water Reactor Sustainability (LWRS) Program pursued the retrieval of aged structural components for the study of the microstructure, mechanical, and corrosion-related properties including stress corrosion cracking (SCC) and irradiation-assisted stress corrosion cracking (IASCC) initiation and growth. To this end, the MRP successfully harvested two high fluence BFBs from a Westinghouse two-loop downflow type PWR in 2016. In the same year, the two BFBs were received at the Westinghouse, Churchill, PA, facility for inspection and specimen fabrication. The fabrication was completed in 2017 with specimens shipped to Oak Ridge National Laboratory (ORNL) for further testing.

In this report, we present our latest study in FY22 on microstructural characterizations of the second high fluence baffle-former bolt, i.e., bolt # 4412. The objective of this project is to provide information that is integral to evaluating end of life microstructure and properties as a benchmark of international models developed for predicting radiation-induced swelling, segregation, precipitation, and mechanical property degradation. Initial characterization focusing on microstructure for one harvested BFB, i.e., bolt #4416 and microhardness on both BFBs has been summarized in the FY19 milestone report for this project [2]. Fracture toughness and fatigue crack growth rate testing results of both BFBs have also been published in the FY21 milestone report [3] for this project. Those initial microstructural characterizations utilized transmission electron microscopy (TEM) and scanning transmission electron microscopy (STEM). Here, in addition to TEM and STEM, further characterization via atom probe tomography (APT) was performed to determine elemental segregation mechanisms with high resolution. Results from this study specifically fill the knowledge gaps for the mechanisms of radiation-induced precipitation and cavity formation as a function of radiation temperature and radiation dose for type 316 austenitic stainless steels used in commercial PWR power plants.

2. EXPERIMENTAL

2.1 Materials

The two harvested BFBs had the highest fluence among bolts withdrawn from service in 2011. Both bolts showed no indication of cracking during the ultrasonic inspection and in visual inspection following removal from service. However, the bolts required a lower torque for removal from the baffle structure than the original torque specified during installation. Figure 2.1 shows images of the bolt heads of two retrieved BFBs. No indication of surface cracking was observed in the transition region between the shaft and head, although some surface debris scale flaked off from the bolt body. The shiny portion of the bolt head was due to electric discharge machining (EDM) when the bolts were removed from the baffle wall. The ID number for the bolts follows a 4-digit code with the first number being the quadrant location in the reactor, then the associated baffle plate number, the column location of the bolt associated with the particular baffle plate number, and finally the former plate location where the bolt originated. Previous reports stated that the bolts are type 347 austenitic stainless steel (SS) [2]. Although the exact elemental compositions of the two retrieved BFBs are also not available. Table 2.1 shows the compositions of three

heats of type 347 SS used for the construction of the reactor in comparison with the material specification. The compositions of all three heats met the type 347 SS specification. However, based on the Scanning Electron Microscopy (SEM)-Energy Dispersive X-ray Spectroscopy (EDS) results, with an example of the EDS spectra in Figure 2.2, obtained in this fiscal year, it was found that the actual material for both bolts was cold-worked type 316 SS instead of type 347 SS due to lack of Nb and existence of Mo in the bolt. The same surprise was found in another bolt from Point Beach Unit 2, a Westinghouse two-loop PWR, as documented in an Electrical Power Research Institute (EPRI) report on hot cell testing of BFBs [4]. The composition in both atomic percent (at%) and weight percent (wt%) for bolt 4412 as determined by atom probe tomography (APT) is presented in Table 2.2. This bolt is within specifications for type 316-SS with slightly elevated Cr content, but this could be due to local variations. This composition from APT further confirms the bolt is of type 316 and not type 347 SS.

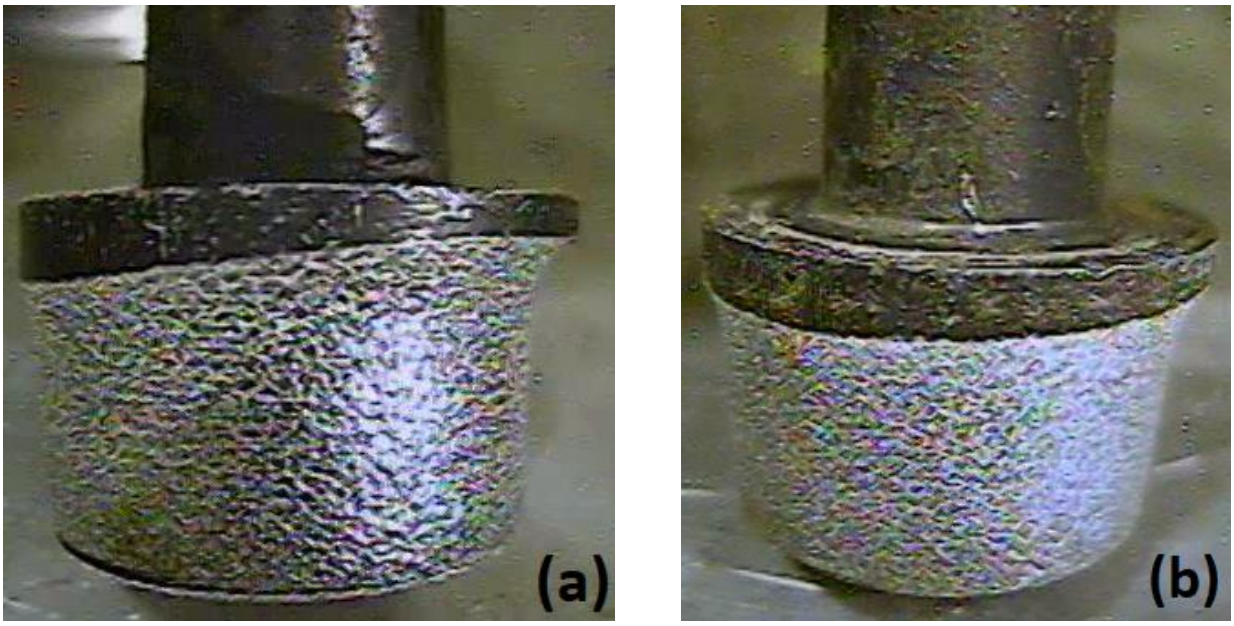

Figure 2.1 Images of bolt heads for bolt #4412 in (a) and bolt #4416 in (b) [5]

Table 2.1 Compositions of three heats of type 347 SS used for the construction of the reactor in comparison with material specification (wt%)

Element	Heat A	Heat B	Heat C	UNS S34700 spec.
Fe	Bal.	Bal.	Bal.	Bal.
Ni	10.46	10.68	9.80	9.00-13.00
Cr	18.10	17.95	18.64	17.00-19.00
Mn	1.63	1.34	1.83	2.00 max
Nb	0.96	0.70	0.81	10 x C min, 1.00 max
Si	0.75	0.55	0.75	1.00 max
C	0.05	0.06	0.07	0.08 max
P	0.03	0.03	0.023	0.045 max
S	0.026	0.02	0.018	0.03 max

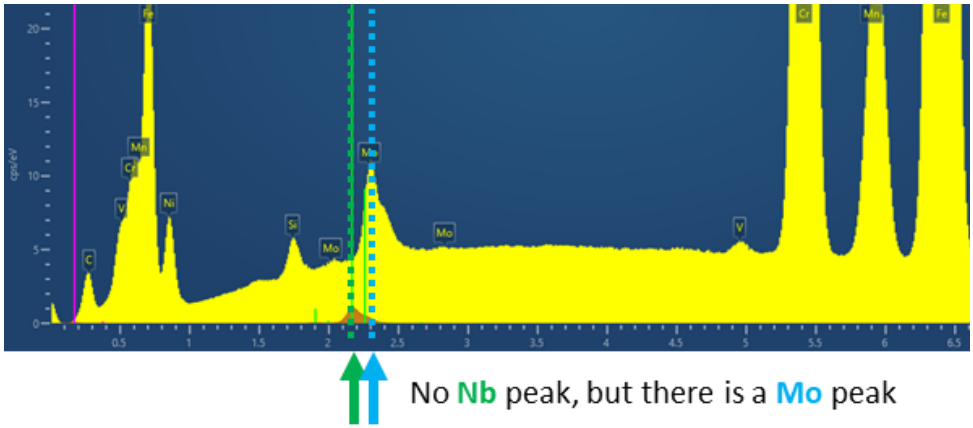

Figure 2.2 SEM-EDS energy spectra of from bolt #4412 (with similar spectra for bolt #4416 not shown) showing a Mo-Lα peak at 2.29 keV but no Nb-Lα peak at 2.17 keV.

Table 2.2 Average compositions of bolt 4412 from 12 APT reconstructions (4 from each section of bolt) in comparison with material specification (wt%) for 316 SS

Element	At%	Wt%	UNS S31600 wt% spec.
Fe	64.19	64.62	Bal.
Ni	11.55	12.22	10.00-14.00
Cr	19.32	18.11	16.00-18.00
Mn	1.62	1.60	2.00 max
Mo	1.18	2.04	2.00-3.00
Si	1.24	0.63	1.00 max
C	0.20	0.043	0.08 max
P	0.024	0.013	0.040 max
S	N/A	N/A	0.030 max
Cu	0.26	0.29	0.75 max

Table 2.3 provides information on the range of fluences and estimated displacement damage along the length of the two bolts. The displacement damage values for the two bolts range from 15 to 41 displacements per atom (dpa) assuming a fluence to dpa conversion value of 6.7×10^{20} n/cm^2, E > 1 MeV per dpa [6]. Other important information for the two retrieved bolts not available at the time of preparation of this report includes the irradiation temperature profile, irradiation flux, and thermomechanical stress state. These require more complicated modeling and calculation and can vary within each power cycle and from cycle to cycle. For instance, calculations [7] from Point Beach Unit 2, which is another Westinghouse two-loop type PWR, showed that the irradiation temperature and flux for a BFB from a region next to the bolt 4416 studied in this work varied in the range of 323-344 °C and 7.5×10^{12}-1.8×10^{13} n/cm^2-sec (E > 1 MeV) along the length of the bolt, respectively. Similarly, a baffle-former bolt removed from the Tihange 1 PWR showed a variation in irradiation temperature of about 23 °C (320-343 °C) along the bolt and a damage dose that was 2.6X higher in the bolt head (19.5 dpa) than the bolt thread (7.5 dpa) [8]. Therefore, the value for a detailed calculation on irradiation temperature and flux of BFBs may be limited due to the large variation of those parameters during the lifetime of a BFB. It is worth noting that Point Beach Unit 2 was originally a Westinghouse two-loop downflow type PWR but was converted to upflow in November 1986 [7].

Table 2.3 Fluence and estimated displacement damage distributions for two retrieved BFBs

Bolt #	Fluence (10^{22} n/cm^2, E > 1 MeV)/Estimated dpa

	Head	Mid-shank	Mid-thread
4412	2.78/41	2.27/34	1.46/22
4416	1.91/29	1.56/23	1.00/15

The specimen machining plan and the schematic for specimen ID are shown in Figure 2.3 and Figure 2.4, respectively. For each BFB, four bend bar specimens and seven thin slice specimens were machined. The bend bar specimens were used in the fracture toughness and fatigue crack growth rate studies, whereas the thin slice specimens are planned for subscale tensile and microstructural analyses. Specimens were machined from different fluence regions of each bolt, allowing for studies of the effect of fluence on the microstructural and mechanical properties of BFBs. Three thin slice specimens were machined from the high-stress concentration region, i.e., the transition between the bolt head and shank, of each bolt to allow for further investigation of possible crack initiation sites.

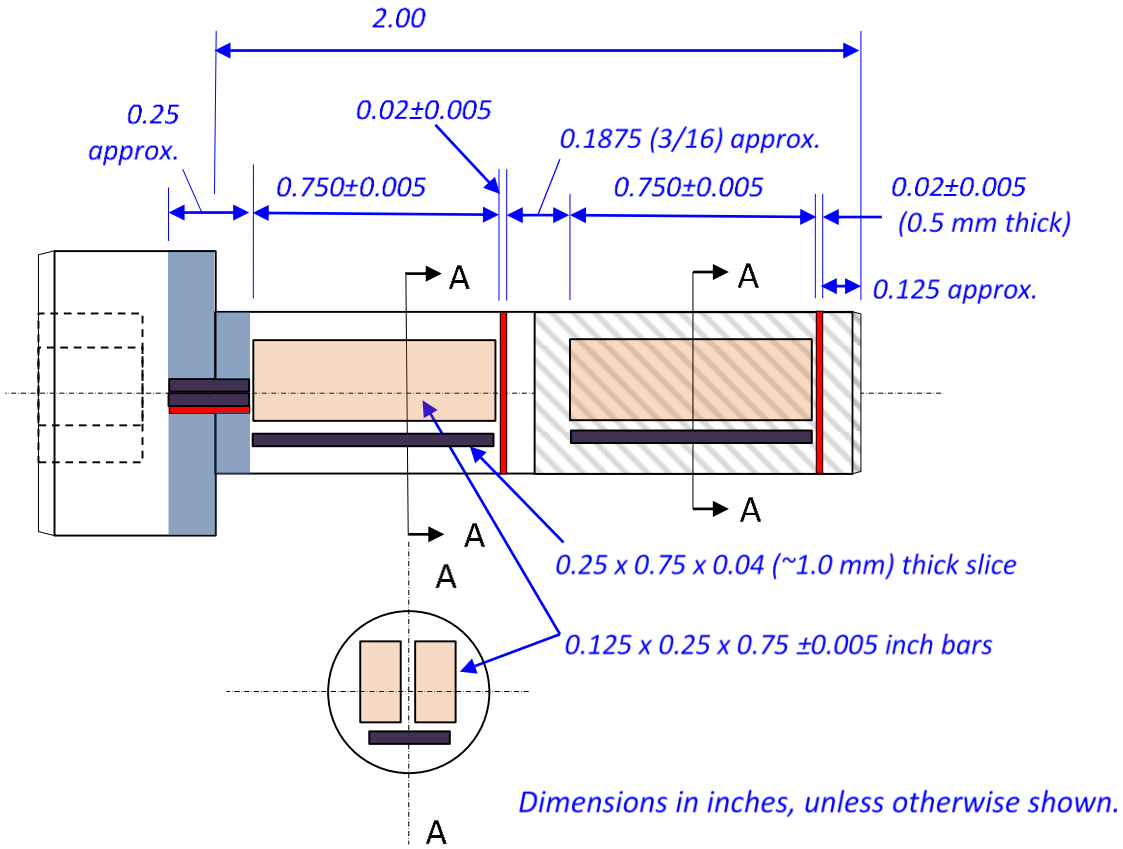

Figure 2.3 Machining diagram for the BFBs showing the color-coded sample types (red: 0.5 mm slices, black: 1.0 mm slices, light orange: bend bars, and light blue: remaining collar materials) [9]

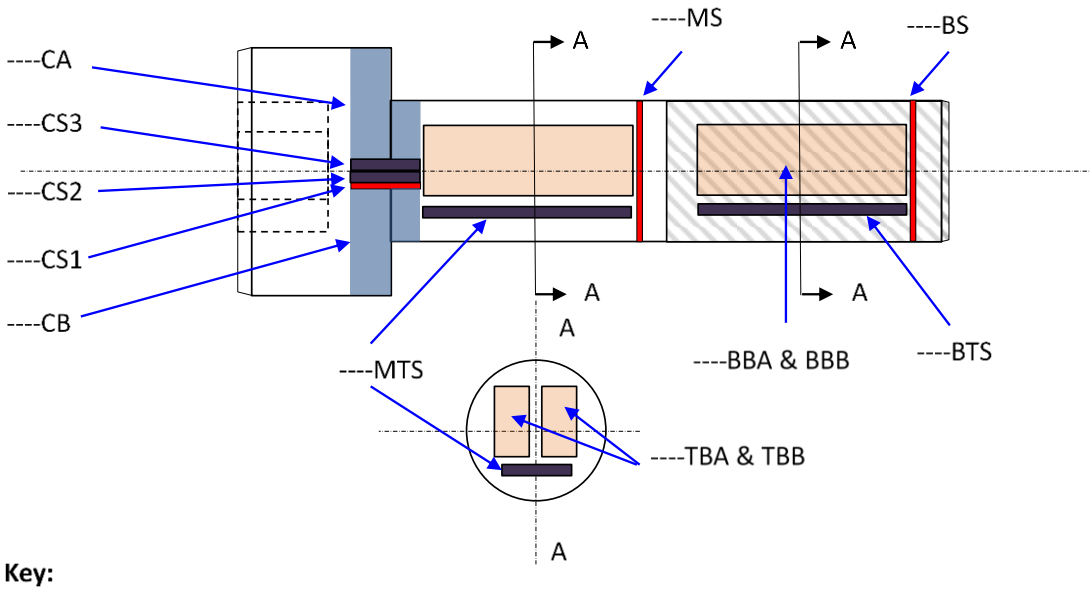

Figure 2.4 Schematic for sample IDs from machined BFBs [9]

2.2 Characterization Methods

Detailed TEM and APT characterizations were performed on the thin slice specimens and needle-shaped specimens prepared by focused-ion-beam/ scanning electron microscopy (FIB/SEM). In detail, after mechanically polished to mirror-surface conditions, thin slice specimens from BS, MS, and CS sections were loaded into an FEI Versa3D FIB/SEM DualBeam™ system, where lamella-type samples were lifted-out from the specimens for TEM characterizations and needle shaped-type speciemns were lifted-out and shaped for APT characterizations. The TEM sample preparation followed the procedures of initial trenching, cutting, and thinning to 200 nm with 30 keV Ga ion beam, rough polishing to 100 nm with ion beam energy gradually reduced from 16 keV to 8 and 5 keV, and fine polishing with 2 keV ion beam to remove most FIB-induced damage. Before loading into the TEM, samples were always cleaned with a Fischione 1020 Plasma Cleaner for 10 minutes on each side using 900 eV Ar ions.

Conventional TEM characterization of radiation-induced dislocation loops and cavities were conducted using a JEOL 2100F field-emission-gun TEM operated at 200 keV. Cavities were identified by comparing underfocused and overfocused images from the same area, providing for quantification of cavity size and distributions. STEM/Energy-dispersive X-ray spectroscopy (EDS)-based mapping was performed using a Thermo (formerly FEI) Talos F200X STEM equipped with the SuperX 4-sector X-ray EDS system. Precipitates and dislocations were imaged using on [001]-zone axis bright field (BF), annular dark field (ADF), and high angle ADF (HAADF) imaging conditions. Beam conditions were ~1-2 nA and 200 keV. X-ray spectrum images were acquired with a rate of ~20,000 counts/second for a duration of about one hour, and then maps of the relevant X-rays lines were extracted via post-processing [10].

APT was performed on a Cameca LEAP 4000XHR using laser pulse mode with a laser energy of 60 pJ, detection rate of 0.005 atoms/pulse, pulse repetition rate of 200 kHz while maintaining needle specimen temperature at ~40 K. Reconstructions and analyses for APT were performed using Cameca's Integrated Visualization and Analysis Software 3.8.10 (IVAS) using techniques that include radial distribution functions (RDF) analysis, frequency distribution analysis, and isoconcentration surface

(isosurface)-based cluster analysis [11–13]. Similar mass/charge range files with only minor adjustments in the widths of selected peaks between reconstructions were used to reduce potential artefacts in compositional analyses among the various samples. The tip profile reconstruction method was used for determining the initial radius of the reconstruction using high resolution SEM images of the final tip. A fixed image compression factor of 1.65 and k-factor of 3.30 was used as no clear pole locations were found within the field ion micrographs. Global background subtraction was used for determining composition. Peak overlaps were considered and adjusted based on relative natural abundance of specific isotopes and preferred evaporation charge state; in general, these overlaps had a minimal effect for the purposes of this study as the greatest overlap accounted for less than 5% of a particular element (isotope 54 with overlaps for Cr and Fe).

Cluster analysis in APT data is a common unsupervised machine learning problem, and like many other problems in this category, it lacks a clear metric/loss function to define a quality of prediction or a confidence level of the result. In this study, we used the isosurface method for Ni, Si, Mo, and Cu clusters identification [14,15]. It is a simple and widely used technique to identify clusters by constructing a constant concentration surface based on local solute concentration, and the enclosed ions are identified as a cluster. This technique has great flexibilities and needs only one user input as concentration threshold. The concentration threshold is kept constant for all datasets since we are interested in the cluster size evolution, which is directly affected by the threshold choice. However, the selection of parameters may lead to some uncertainties for cluster identification in conditions where precipitation is low (i.e., low temperature thermal aging or irradiation). This is due to some clusters having much lower solute concentration in these conditions. However, we believe the corresponding volume fraction trend is preserved despite the minor uncertainties.

RDF analyses of individual elements in APT data enables understanding of not only the extent with which the elements segregate but also to which other elements they are most strongly attracted to or repulsed by [13,16]. RDF analysis provides an average radial concentration around each atom in the APT reconstruction data for a particular element as a function of radial distance from the center atom. This average radial concentration profile for each element, when divided by the average bulk concentration of that element, provides the bulk normalized concentration plots. A value of 1 for bulk normalized concentration corresponds to a random distribution or no correlation with the designated element. A value above 1 indicates attraction with the “center atom” element. A value less than 1 indicates a repulsive interaction with the designated element.

3. RESULTS AND DISCUSSION

3.1 TEM/ STEM Characterization

TEM and STEM characterization revealed heavily evolved microstructures in the BS and CS1-1 sections of the BFB #4412 during service, with high densities of dislocations, precipitation, and cavity formation. These same behaviors were seen previously in the other BFB, #4416 analyzed previously [2]. The STEM BF, ADF, and HAADF imaging and STEM-EDS element maps in Figure 3.1, Figure 3.2, and Figure 3.3 show a high degree of Ni/Si precipitation within the grain interiors. In these observations, no segregation was found at the grain boundaries that were investigated. However, it is highly likely that these boundaries are low angle grain boundaries (LAGB) or twin boundaries; each of which have been shown to have less radiation-induced segregation (RIS) than high angle grain boundaries [17]. This difference between LAGB and HAGB segregation was also found in BFB #4416 [2], so it is expected that RIS will be clearly shown in HAGB in BFB #4412. Interestingly though, in the grain boundary in the BS section in Figure 3.1, there is larger precipitation of Ni/Si/Mn precipitates. The composition line profile through these grain boundary precipitates shows these are a different composition from the Ni/Si precipitates and have a

composition ratio similar to that of G-phase ($Ni_{16}Si_7Mn_6$) often found during aging or irradiation of the ferrite phase in cast austenitic or duplex stainless steels [18,19].

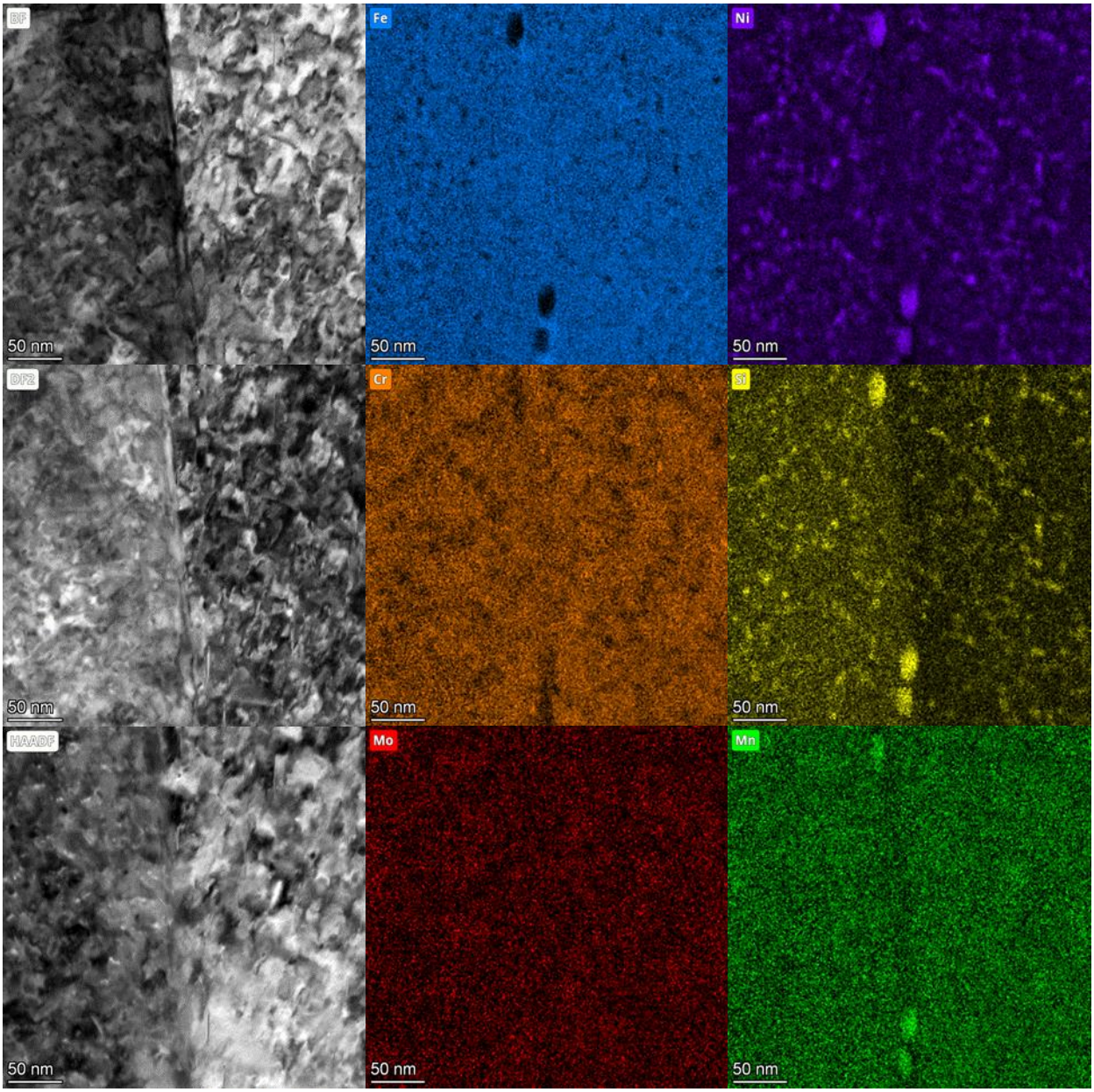

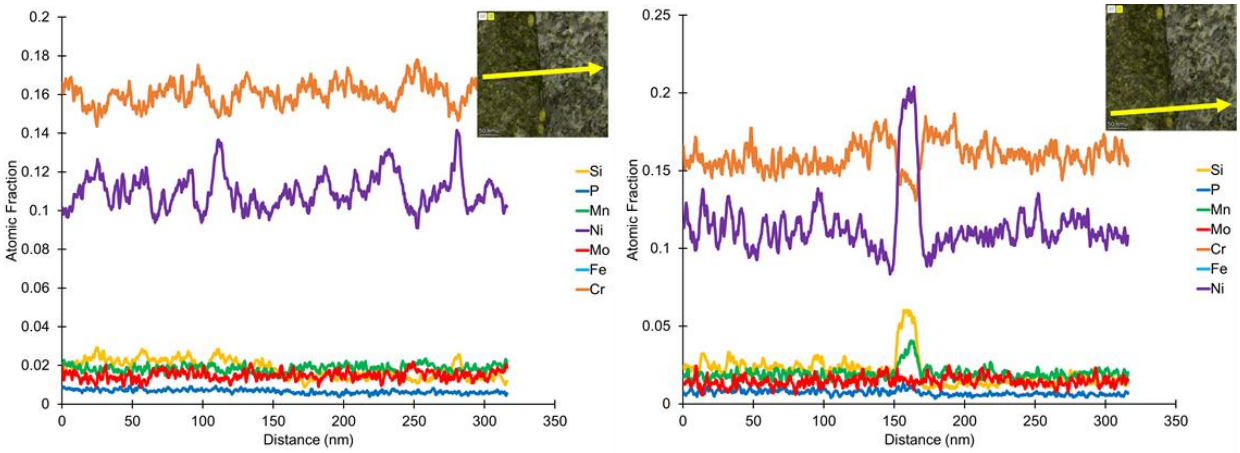

Figure 3.1 STEM-BF/ADF/HAADF images, STEM-EDS element maps, and concentration profiles across a grain boundary (possibly a low angle grain boundary) from the BS section of the BFB #4412.

Separate from the grain boundary, there appears to be a stark difference in the precipitation behavior between the BS and CS1-1 sections of BFB #4412. Comparing the Ni and Si element maps in Figure 3.2 and Figure 3.3, which are at the same magnification near similar twin boundaries, it becomes clear that the number density of Ni/Si precipitates is higher in the CS1-1 section (Figure 3.3) than in the BS section (Figure 3.2). The number density is about 1.5-2 times higher in the CS1-1 section; however quantification is not optimal for EDS of such fine-scale particles (APT in the next section is better for this). The higher number density in CS1-1 makes sense as the radiation dose in the CS1-1 section is approximately double that of the BS section of the bolt. On the other hand, the number density and size appear approximately similar to the corresponding sections from the BFB #4416, which had a lower radiation dose; thus, it is likely that a steady-state or plateau in particle size has been reached and with the size and number density determined by the radiation temperature or strain gradient, with higher density of smaller precipitates occurring at a lower temperature or lower strain. Quantitative instead of purely qualitative comparisons in the number density and size between the two bolts will be determined based on the further APT and STEM analysis to come in FY23. In addition, it appears there is more localized Cr and Mo segregation in the BS section (Figure 3.2) than in the CS1-1 section (Figure 3.3). This highlights that there is a difference other than radiation dose between the bolt head, CS1-1, and the bolt thread, BS. This difference is further emphasized by looking at the difference in cavity size and density.

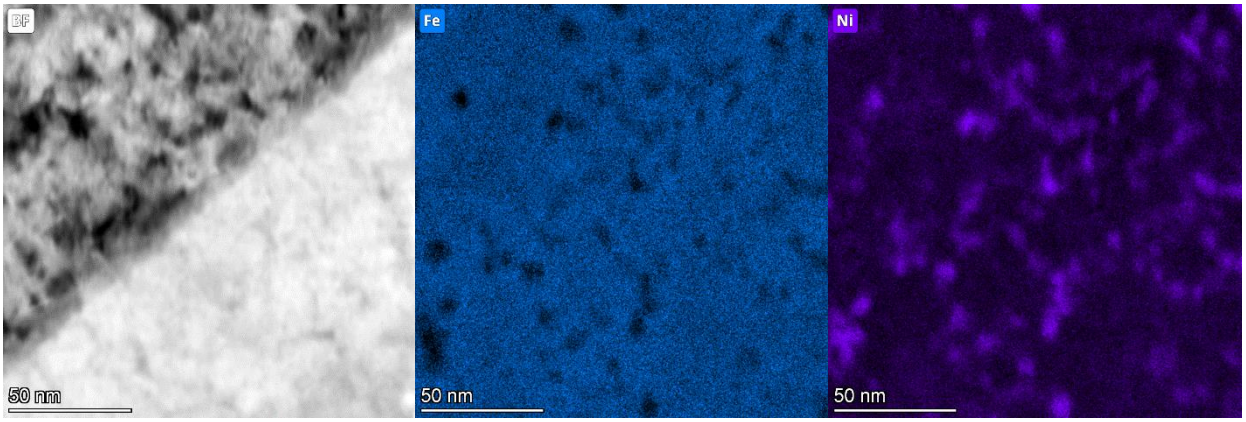

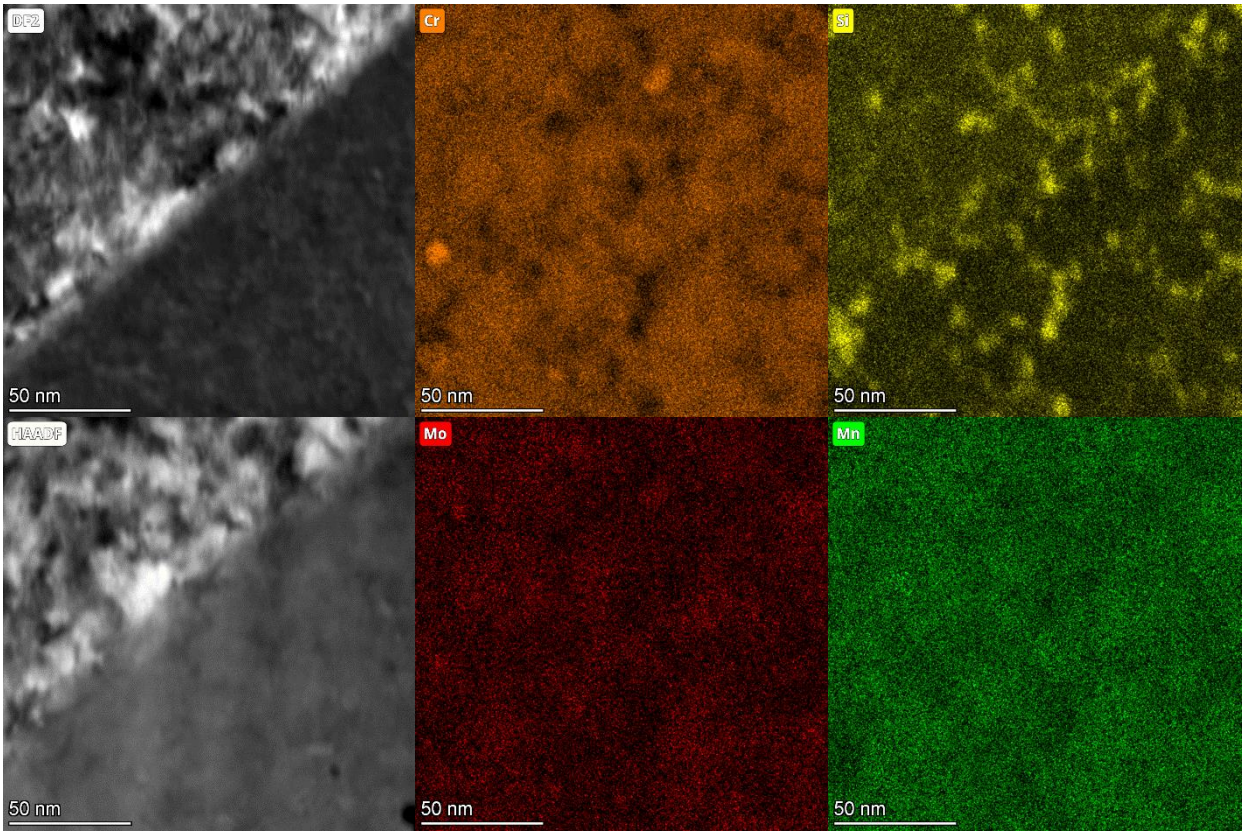

Figure 3.2 STEM-BF/ADF/HAADF images and STEM-EDS element maps at a grain boundary (possibly a twin boundary) from the BS section of the BFB #4412.

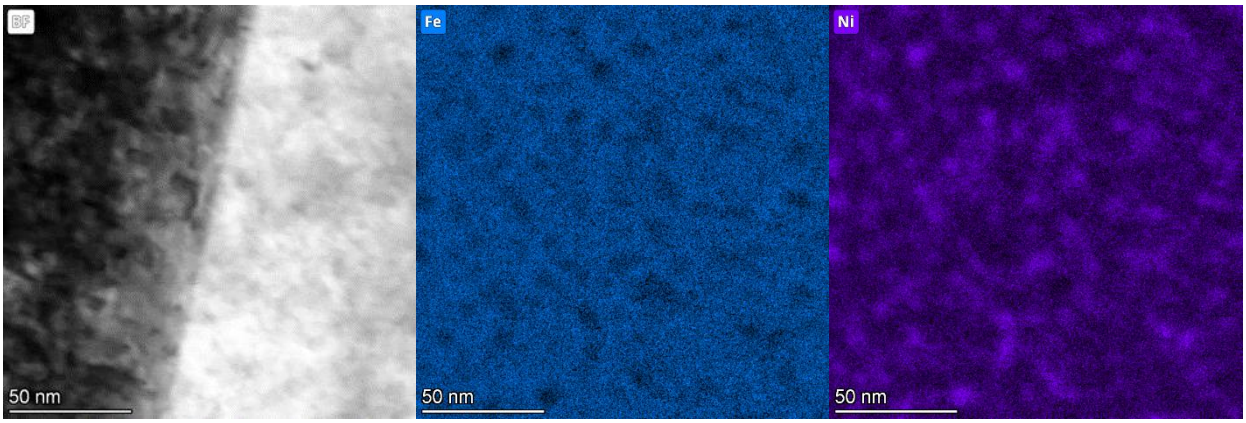

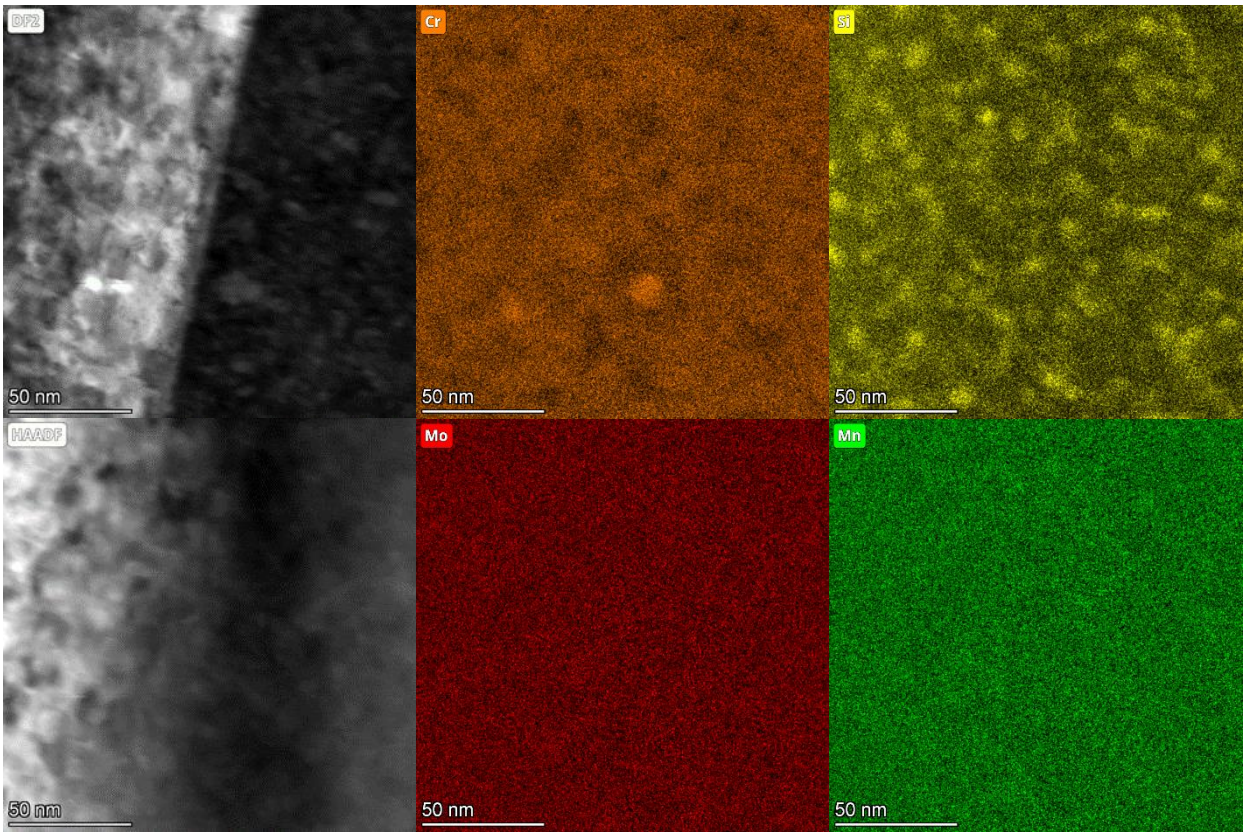

Figure 3.3 STEM-BF/ADF/HAADF images and STEM-EDS element maps at a grain boundary (possibly a twin boundary) from the CS1-1 section of the BFB #4412.

Figure 3.4 shows under-focus TEM images of the BS section (a, b, c) and CS1-1 section of the BFB #4412. The BS section has a bimodal distribution of large cavities – as indicated by blue arrows, ~8 nm in diameter – and small cavities – as indicated by red arrows, ~2 nm in diameter, while the CS1-1 section only has a high density of small cavities (~2 nm in diameter). The larger cavities are indicative of gradients in temperature, strain, fast/thermal neturon energy, and potentially hydrogen concentration from transmutation or exposure to PWR water [20], with each of these being higher in the bolt thread section (BS) than in the bolt head section (CS1-1). Vacancies, along with an abundance of hydrogen, are much more mobile due to thermal and strain gradients where they can gather into vacancy clusters and grow into large cavities that could be gas-filled. This is consistent with what was seen in the BFB #4416 [2], with analysis of a baffle-former bolt retrieved from the Tihange 1 reactor [8], and with variation in void swelling in thick components [21]. The large amount of hydrogen together with transmutant helium [22,23] may together stabilize cavities and lead to growth. Interestingly, within 50-150 nm of the grain boundary in the BS section, there are much fewer large cavities. This denuded zone, as indicated by the yellow arrows, shows the influence of the grain boundary as a sink for defects, consistent with neutron irradiated 316 stainless steel studied elsewhere [24]. This grain boundary is the same one from Figure 3.1; thus, it could be a low angle grain boundary. More work is needed to confirm if the grain boundary character has an effect on the cavity grain boundary denuded zone. Further work is needed to show how this translates to the middle section of the bolt, MS. Also, further STEM and TEM work will investigate the dislocation loop density and size, which is clearly high based on the STEM images in Figure 3.1, Figure 3.2, and Figure 3.3.

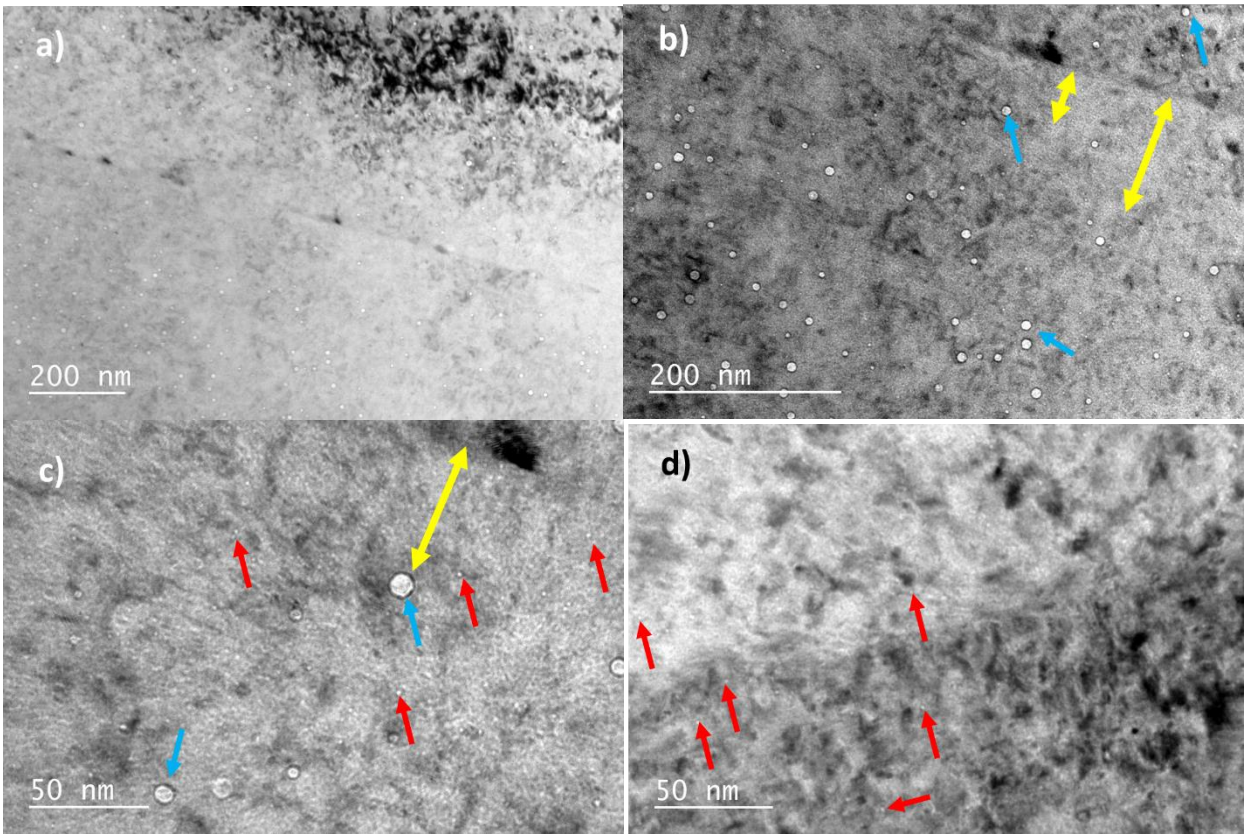

Figure 3.4 Under-focus TEM images showing nano-scale cavities near grain boundaries (possibly a low angle or twin boundaries) from the BS section (a,b,c) and from the CS1-1 section (d) of the BFB #4412.

3.2 APT Characterization

APT characterization was used to complement the TEM/STEM characterization, as it is a technique that enables higher spatial and, in particular, compositional resolution all in three spatial dimensions. Here, APT data was collected from the matrix of four sharpened tips from each of the three sections in the BFB #4412: BS, MS, and CS1-1. Future work will target the grain boundaries in these sections. First, the atomic and isosurface reconstructions will be shown followed by analytical information to determine trends in elemental segregation. Figure 3.5 and Figure 3.6 depict atom reconstructions and isosurface reconstructions, respectively, from one reconstruction of each section of the BFB #4412. Looking at the matrix in Figure 3.5, it appears that Ni, Si, and Mo are faintest in the BS reconstruction, while Cu is faintest in the CS1-1 reconstruction. This partially shows which precipitates form and under what conditions (Ni/Si and Mo preferentially in BS, and Cu in CS1-1). The isosurface reconstructions in Figure 3.6 show similar trends; there appears to be a larger fraction of Ni/Si precipitation in the BS and MS reconstructions than in the CS1-1 (as the green and gray isosurfaces strongly overlap). However, the number density of small Ni/Si precipitates appears larger in the CS1-1; a point confirmed in Figure 3.7. The red Mo and orange Cu isosurfaces are slightly separate from the Ni/Si isosurfaces. Though to be clear, not all Ni/Si isosurfaces have Mo or Cu isosurfaces attached to them.

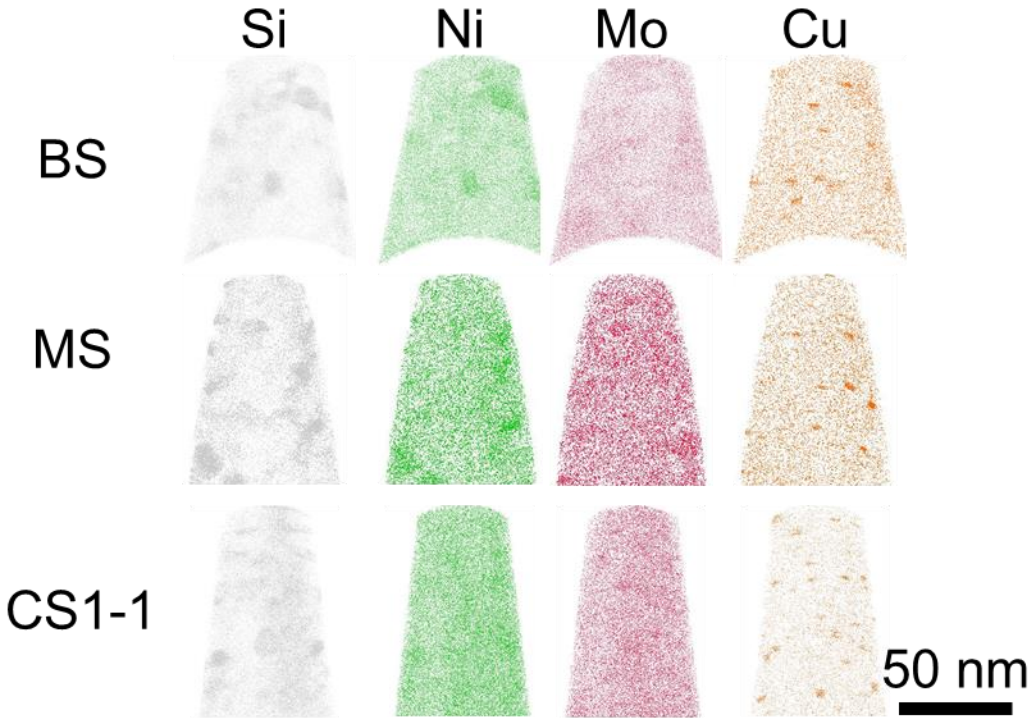

Figure 3.5 Atom reconstructions of Si, Ni, Mo, and Cu atoms from a select reconstruction of each section of the BFB #4412 – BS, MS, and CS1-1. The reconstructions here are 30 nm in thickness.

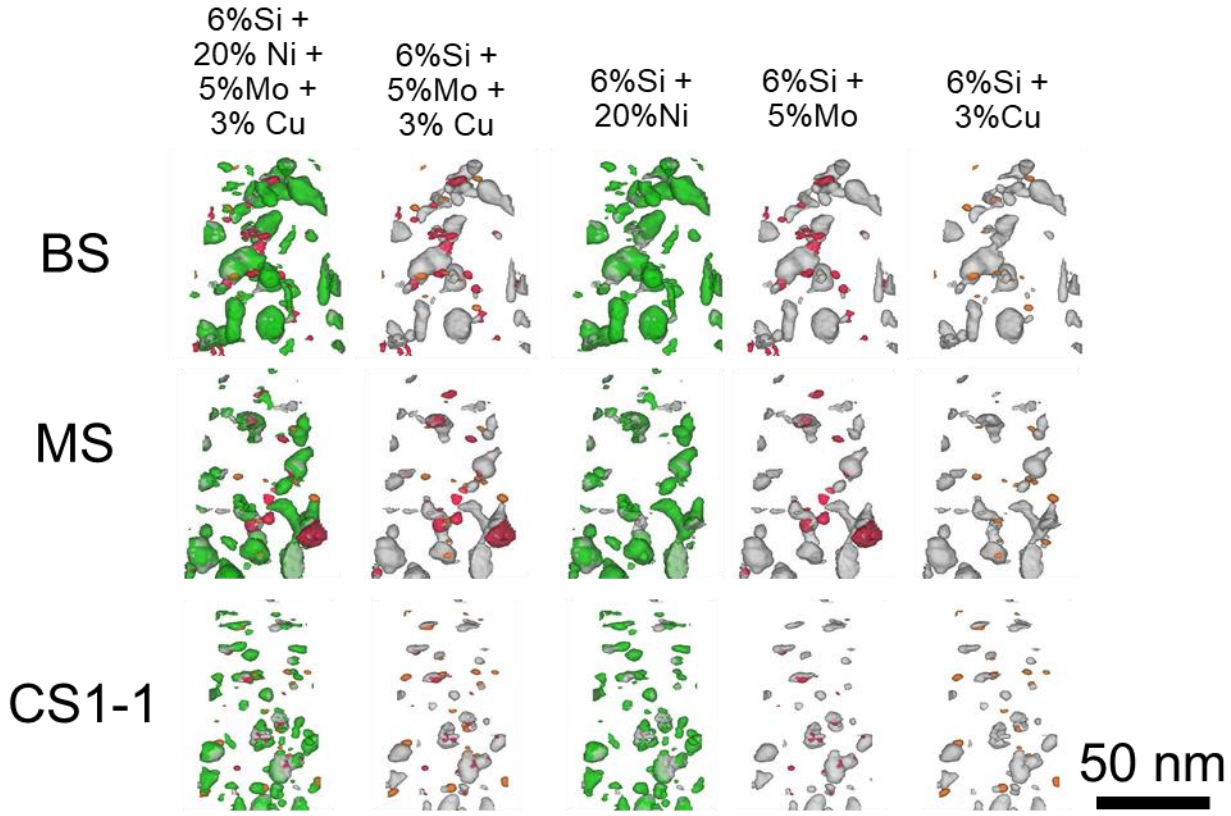

Figure 3.6 Isoconcentration surface (isosurface) reconstructions of same regions as in Figure 3.1, though through the full thickness of the reconstruction. Green isosurfaces are of 20at% Ni, gray isosurfaces are of 6at% Si, red isosurfaces are of 5at% Mo, and orange isosurfaces are of 3at% Cu.

APT characterization allows for a high degree of quantification beyond standard visualization. Figure 3.7 shows the volume fraction, average spherical-equivalent radius, and number density of Ni-20at%, Si-6at%, Mo-5at%, and Cu-3at% isosurfaces averaged over the four reconstructions from each section of the BFB #4412. The volume fraction of Ni and Si isosurfaces is highest in the BS section and lowest in the CS1-1 section, while the opposite is true for the number density. The average radius follows a similar trend as volume fraction for the Ni and Si isosurfaces, but the BS and MS sections have similar sizes. The Mo isosurfaces appear to have no trends in volume fraction, radius, or number density, each also with a high degree of variation. On the other hand, the volume fraction and number density of Cu isosurfaces is highest in the CS1-1 section compared to the BS and MS sections.

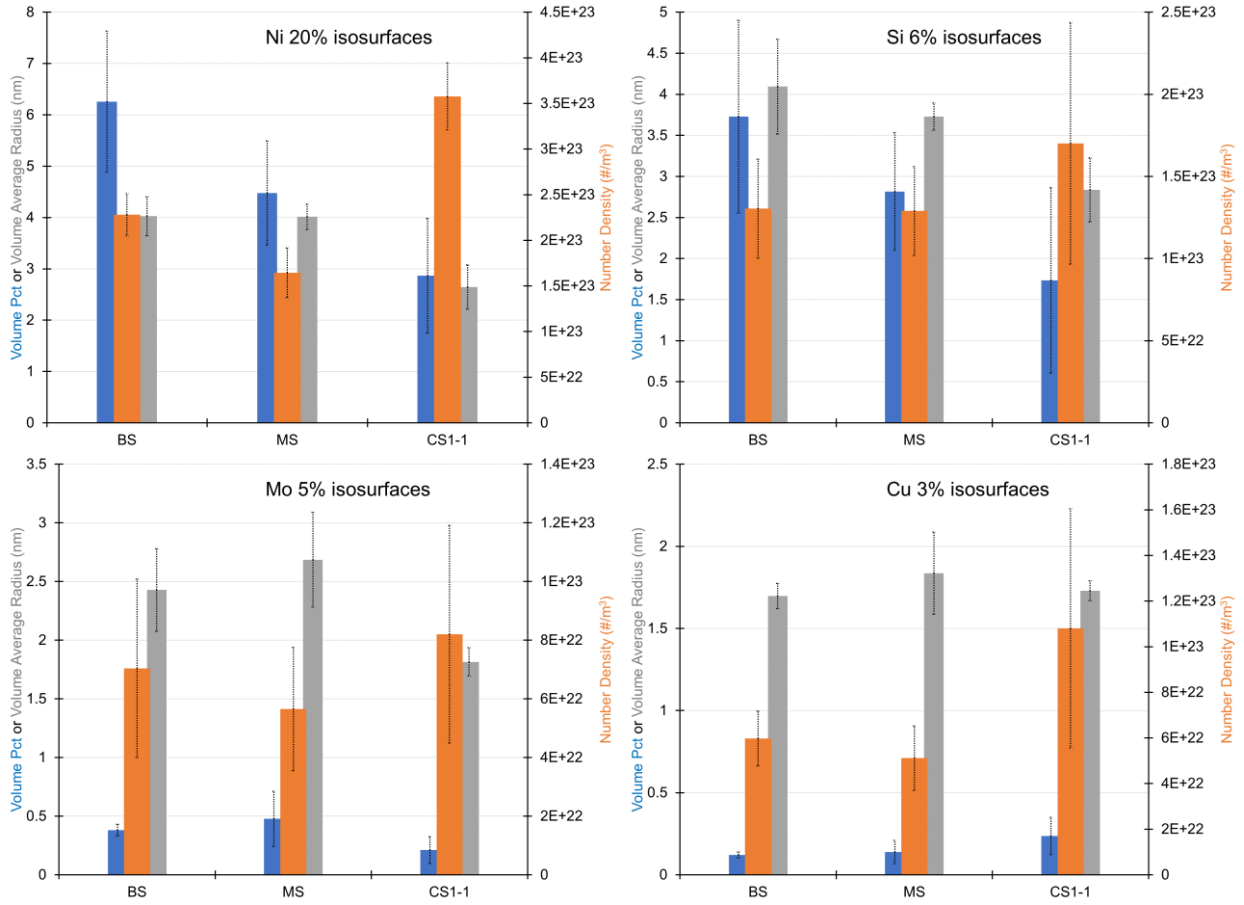

Figure 3.7 Volume percent (in blue), volumetric average spherical equivalent radius (in gray), and number density (in orange) of 20at% Ni, 6at% Si, 5at% Mo, and 3at% Cu isosurfaces averaged over four reconstructions for each section of the BFB #4412. Error bars represent one standard deviation.

As depicted in Figure 3.6, it is clear that precipitates of different compositions form adjacent to each other. Ni/Si isosurfaces form the largest clusters while Mo and Cu surfaces are present on opposite sides of the main Ni/Si surfaces. APT allows for determining the concentration distribution near and through these isosurfaces. Figure 3.8 shows the 2D concentration contour plots and 1D concentration profile in the plane of a Cu/Si/Mo isosurface from a reconstruction of a tip in section BS of the BFB #4412. There is a center Ni/Si-rich precipitate with a size of about 10 nm that has a composition similar to Ni_3Si with a

Cu-rich precipitate on the left side and a Cr/Mo/P-rich precipitate on the right side. Mn does not segregate into the precipitates but remains in the matrix; as such, it is clear that the matrix precipitates are not G-phase that is similarly found in aged or irradiated ferritic steels. The Cr/Mo/P-rich phase could be an α` domain. Interestingly, co-precipitates of Cu/Ni-Si-Mn/Mo were identified in thermally aged ferrite in duplex stainless steels [15], and co-precipitates of Cu-Ni-Si/Mo-Cr were found in 304 austenitic stainless steel retrieved from a commercial BWR power plant [25]. However, no tri-precipitates of Cu/Ni-Si/Mo-Cr-(P) without Mn in the Ni/Si phase have been observed to our knowledge in thermally aged or irradiated 304/316 type austenitic stainless steels.

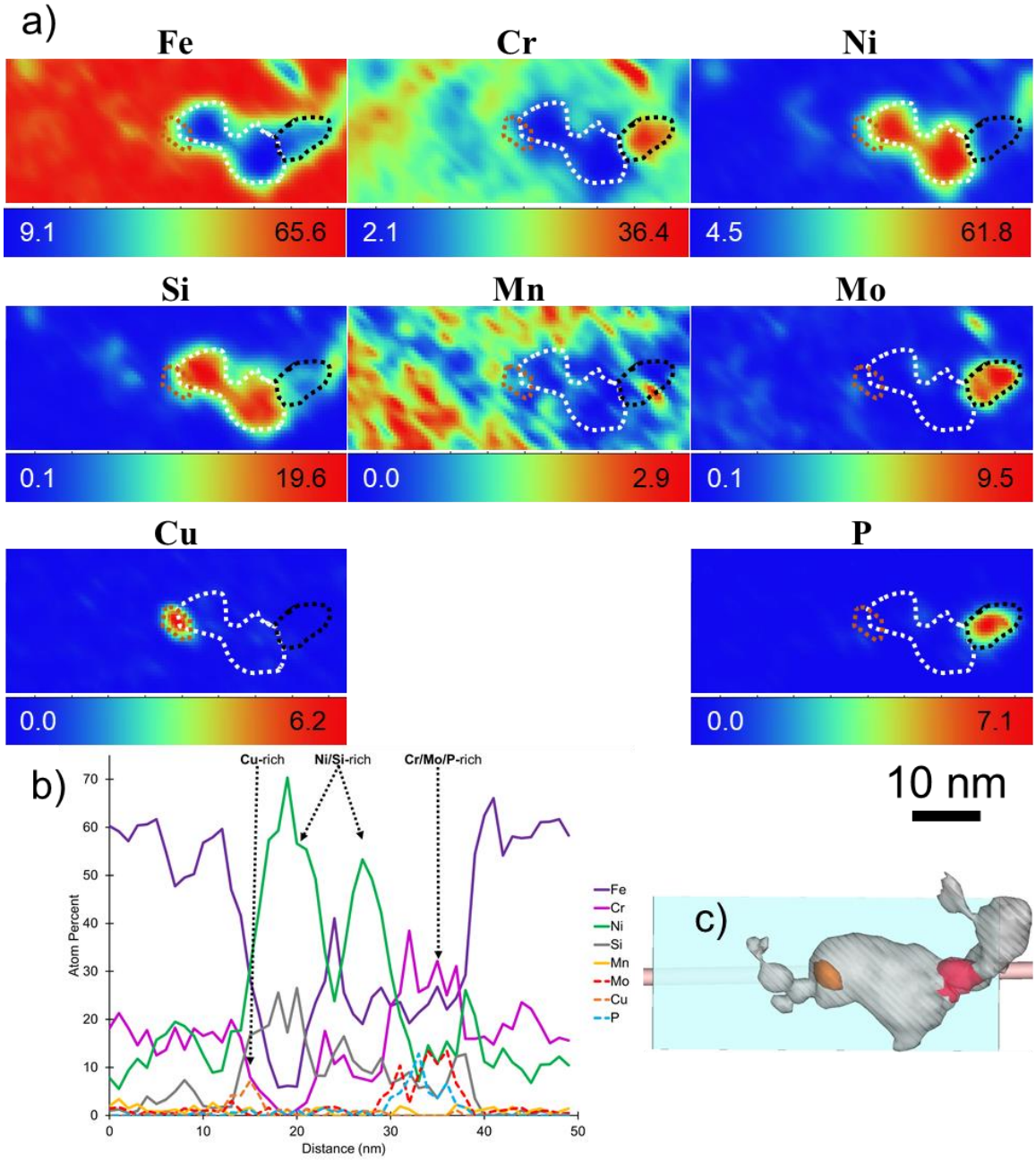

Figure 3.8 a) 2D concentration contour plots and b) 1D concentration profile through a co-precipitate of a Cu-rich precipitate adjacent to a Ni/Si-rich precipitate adjacent to a Cr/Mo/P-rich precipitate from section BS of the BFB #4412 (same reconstruction in Figure 3.5 and Figure 3.6). White dots encircle the Ni/Si-rich

cluster, black dots encircle the Cr/Mo/P-rich cluster, and orange dots encircle the Cu-rich cluster. c) Cu, Si, and Mo isosurfaces with box and cylinder from which a) and b) are taken from.

As mentioned in section 2.2, using isosurfaces to determine clustering is imprecise and depends on an arbitrary at% input and on the quality of the reconstruction as clustering is highly localized. To remove some of the arbitrariness and still identify and determine trends, frequency distribution analysis (Figure 3.9) and radial distribution function analysis (Figure 3.10, Figure 3.11, and Figure 3.12) were performed. Frequency distribution analysis groups together atoms into bins of in this case 200 atoms, calculates the concentration of each element in those bins, and then determines the frequency of a given concentration over the entire reconstruction. After phase separation as a result of irradiation, the shape of the peaks change relative to binomial distribution, as shown in Figure 3.9a, with some bins becoming purer in Fe, while others become more concentrated in Ni, Si, or Cu. Furthermore, Pearson correlation coefficient analysis uses the frequency distributions to identify the degree of phase separation. The Pearson correlation coefficient (μ) is based on the chi square ($\chi 2$) test with datasets that vary in size, which is useful here as the APT reconstructions are not of the same size for the different reconstructions [12]. Figure 3.9b shows the Pearson correlation coefficient for Fe, Cr, Ni, Si, Mn, Mo, and Cu. The value of μ is between 0 and 1, with 0 corresponding to fully homogeneous and 1 to a high degree of phase separation. Based on this, it is clear that Fe, Cr, Ni, Si, and Mo have more elemental segregation in the BS and MS sections of the bolt than in the CS1-1 section of the bolt. On the other hand, Cu has more elemental separation in the CS1-1 section of the bolt than the BS and MS sections.

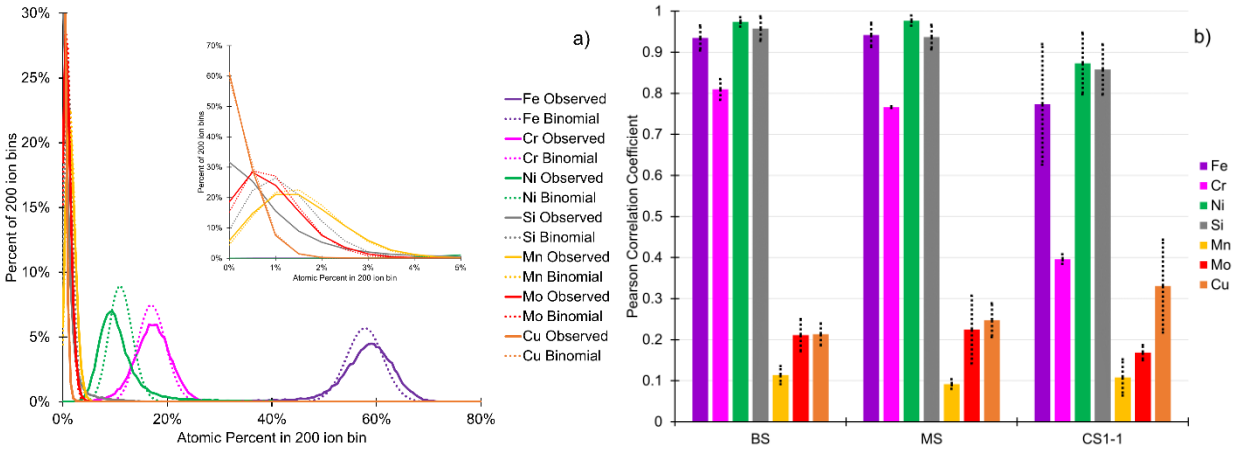

Figure 3.9 a) Example frequency distribution of 200-ion bins and binomial distribution of elements based on reconstruction concentration from BS tip 3. b) Pearson correlation coefficients of Fe, Cr, Ni, Si, Mn, Mo, and Cu atoms averaged over four reconstructions for each section of the BFB #4412, based on doing frequency distribution analysis. Error bars represent one standard deviation.

Taking the frequency distribution analysis further, radial distribution function analysis shows the degree of elemental separation and which elements they segregate to or from over the entire reconstructions as Figure 3.10, Figure 3.11, and Figure 3.12 present the bulk normalized concentration of certain elements as a function of distance from Ni, Mo, and Cu atoms, respecitvely. Values greater than 1 indicate attraction and values less than 1 indicate repulsion. Looking at the concentration near Ni atoms in Figure 3.10, Ni and Si segregation to Ni atoms is higher in the BS section, which likely has a higher irradiation temperature, than the CS1-1 section despite it having a higher dose. Separation of Cr and Mo from Ni atoms follows the same trend of BS > MS > CS1-1. Interestingly though, Cu has no particular trend toward Ni atoms as the variation between tips effectively makes them all the same. In Figure 3.11, segregation of Mo away from Ni and towards Mo and Cr confirms what was seen in the 2D concentration contour plots in Figure 3.8 and in the STEM-EDS maps in Figure 3.2. The same trend for Ni/Si is also found for Mo, where the BS section has more elemental segregation than the MS and CS1-1 sections; though BS and MS are more similar.

Lastly, in Figure 3.12, Cu segregation to Ni is modest and follows no trends, but Cu segregation to itself is high and follows the inverse trend of Ni/Si/Mo, where CS1-1 has by far the greatest degree of elemental segregation for Cu. These competing results show that the size of the Cu precipitates remain small whether or not Ni/Si precipitates have formed to a large degre. This confirms the insights gained from the isosurface analysis.

The Cu clustering may have a higher dependence on radiation dose than on temperature as Cu is likely to phase separate at any elevated temperature due to its low miscibility in Fe and Cr. Thus, Cu precipitation has a higher dependency on vacancy concentration than on vacancy or atomic mobility, whereas Ni/Si precipitation may have the opposite dependency. This makes sense as the miscibility of Cu in many metals is quite low, and therefore, the activation energy to phase separate for Cu is not high [26]. On the other hand, the solubility of Ni and Si in FCC Fe is higher; therefore, more energy in the form of thermal energy is needed to cause phase separation. Ballistic mixing during radiation generally favors dissolution of Ni and Si into FCC Fe, while the thermal spikes during irradiation are enough to cause Cu precipitation, independent of temperature, but as the temperature rises, ballistic mixing of Ni and Si is overcome by back diffusion due to a bias for phase separation [27]. In comparison with the BFB #4416, which has a lower overall radiation dose, it is expected that the volume fraction and number density would be similar or slightly lower for the Cu clusters, while the Ni/Si-rich clusters will likely have a smaller radius but similar number density. This would be consistent with Cu-rich precipitation and Mn-Ni-Si-rich precipitation in reactor pressure vessel steels [28,29]. The APT data collection for BFB #4416 will come in the next fiscal year.

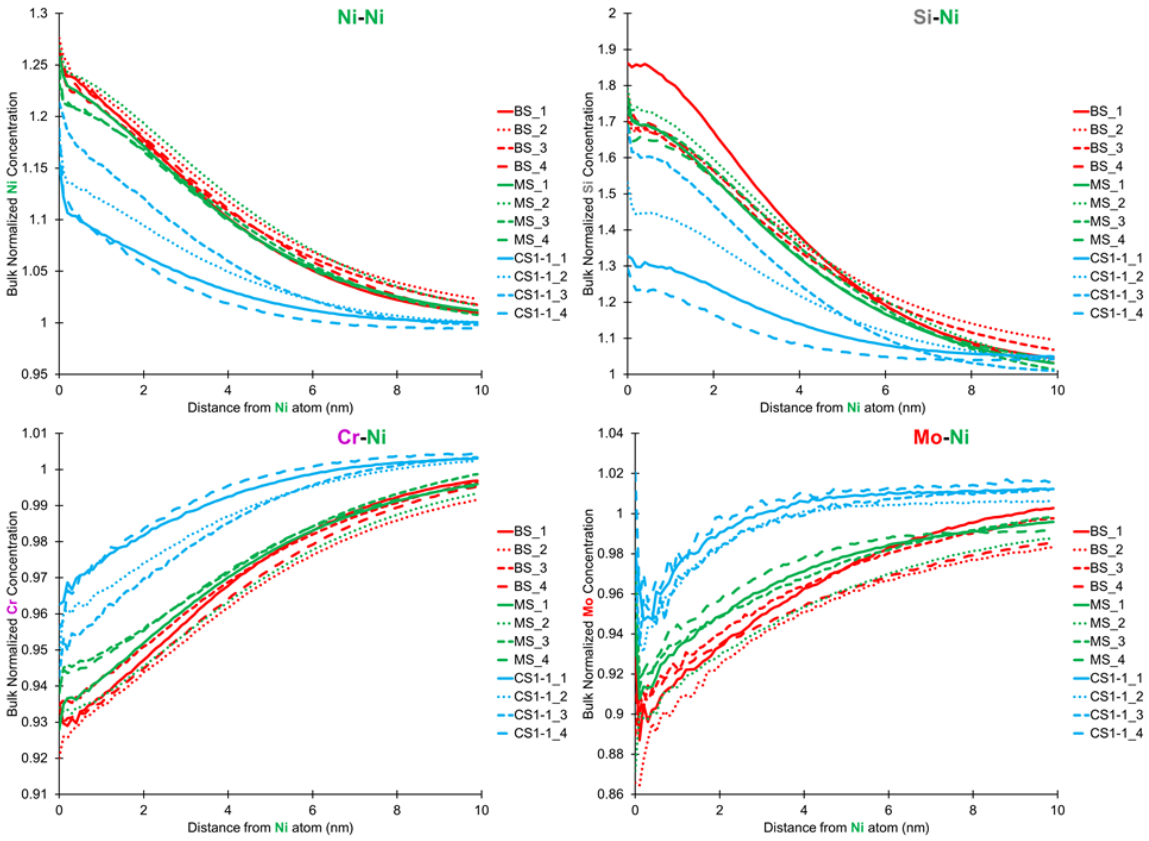

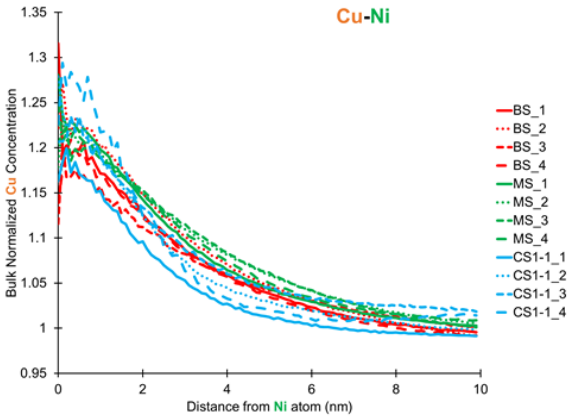

Figure 3.10 Bulk normalized Ni, Si, Cr, Mo, and Cu concentrations as a function of distance from a generic Ni atom for each of the four reconstructions for each section of the BFB #4412 (marked as _1, _2, _3, and _4, respectively), based on doing radial distribution function (RDF) analysis.

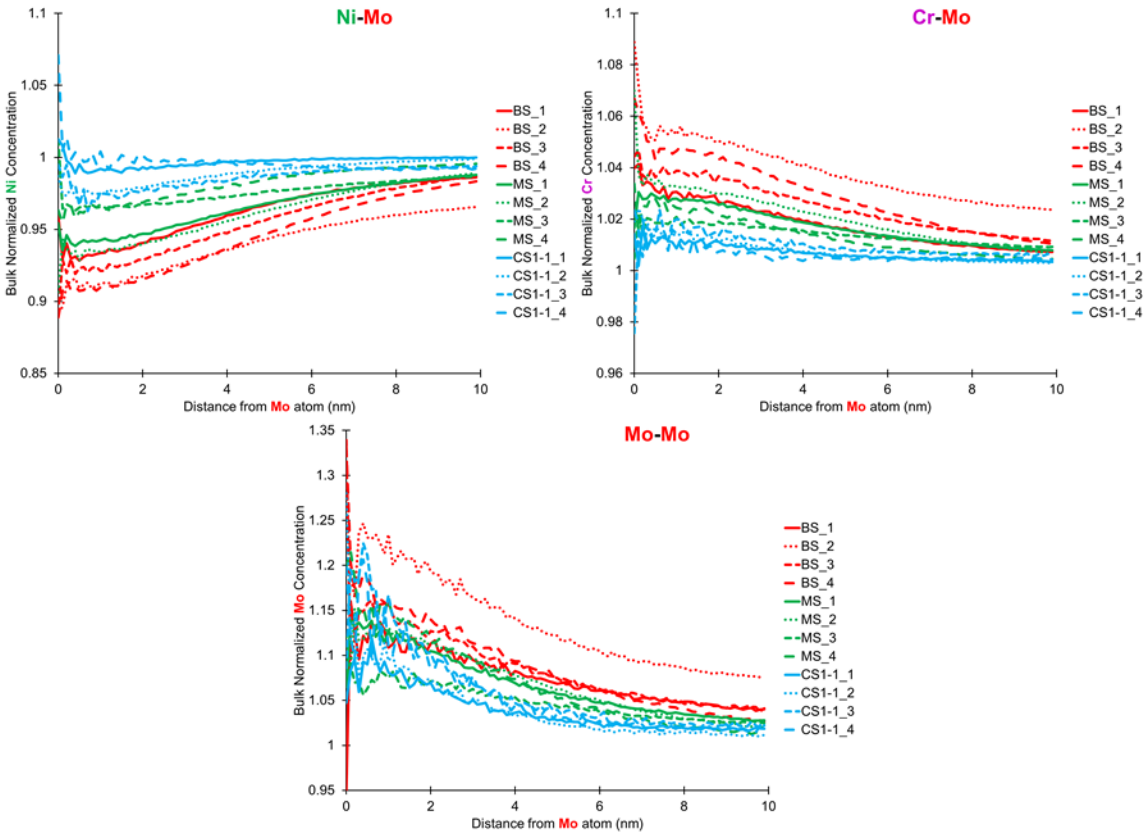

Figure 3.11 Bulk normalized Ni, Cr, and Mo concentrations as a function of distance from a generic Mo atom for each of the four reconstructions for each section of the BFB #4412 (marked as _1, _2, _3, and _4, respectively), based on doing radial distribution function (RDF) analysis.

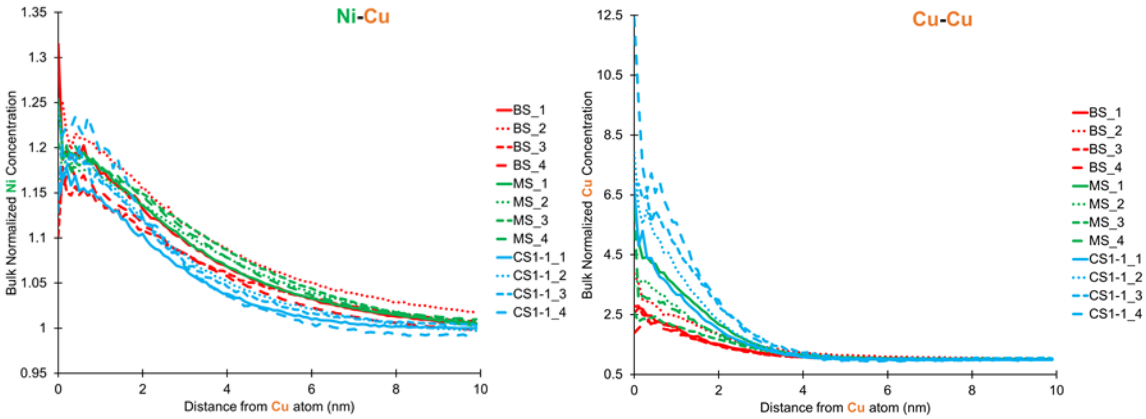

Figure 3.12 Bulk normalized Ni and Cu concentrations as a function of distance from a generic Cu atom for each of the four reconstructions for each section of the BFB #4412 (marked as _1, _2, _3, and _4, respectively), based on doing radial distribution function (RDF) analysis.

4. CONCLUSIONS

In this report, we present our latest study in FY22 on microstructural characterization of the second high fluence baffle-former bolt, i.e., bolt # 4412, harvested from a commercial Westinghouse two-loop downflow type PWR using both TEM/STEM and APT. The objective of this project is to provide information that is integral to evaluating end of life microstructure and properties as a benchmark of international models developed for predicting radiation-induced swelling, segregation, precipitation, and mechanical property degradation. The main findings are summarized as follows:

1) The cavity size was considerably larger in the bolt thread section than in the bolt head, with the bolt thread section having a bimodal distribution of cavities greater than ~6 nm in diameter and less than ~3 nm in diameter. The bolt head only had the small-sized cavities. This is consistent with the previously characterized bolt #4416. In addition, there was a denuded zone of large cavities near grain boundaries in the thread section of the bolt.
2) Radiation-induced precipitation in the BFB #4412 was highly complex, with the volume fraction, size, and number density of Ni/Si and Cu-rich precipitates depending strongly on the radiation temperature/dose. In the previous study of bolt #4416 [2], using just STEM-EDS, only Ni/Si-rich preciptiates were identified. Here, multi-phase precipitates were identified using APT, in which co-precipitates of adjoined clusters were found with Ni/Si-rich precipitates sandwiched between Cu-rich clusters and Cr/Mo/P-rich clusters. Ni/Si-rich clusters had a higher volume fraction in the thread sections of the bolt compared to the bolt head section, while the reverse was true for Cu-rich clusters. Ni and Si were attracted to themselves and Cu while rejecting Cr and Mo. Mo preferentially segregated to itself and Cr. Cu, while being attracted to Ni and Si, had a much higher attraction to itself; consistent with the three sets of clusters that were observed.
3) Solute segregation out of solution was highest for most solute elements in the thread section of the bolt #4412 with the exception of Cu, which experienced more separation out of solution into Cu-rich clusters in the bolt head section. This highlights the difference in the mechanisms for precipitation of Ni/Si clusters, which have the Ni_3Si phase composition and precipitation of Cu-rich clusters. The immiscibility of Cu in FCC Fe favors lower temperature phase separation, while competition between ballistic mixing and thermal phase separation is more apparent for Ni/Si.
4) Gradients in temperature, strain, neutron energy spectrum, and hydrogen concentration likely affect the microstructural variation along the length of the bolt that overcomes the ~2X difference in irradiation dose that between the bolt head and the bolt thread. The irradiation temperature,

thermal/fast neutron ratio variation, potential strain gradient, and exposure to PWR coolant water that each section of the bolt sees may have more influence on the microstructural evolution than the total irradiation dose. The bolt thread and shank, with higher temperature, higher relative fast neutron flux, higher strain, and exposure to coolant but lower dose, underwent more enhanced cavity formation, precipitation, and solute segregation than the bolt head section.

5. REFERENCES

[1] Stress Corrosion Cracking in Light Water Reactors: Good Practices and Lessons Learned, INTERNATIONAL ATOMIC ENERGY AGENCY, Vienna, 2011. https://www.iaea.org/publications/8671/stress-corrosion-cracking-in-light-water-reactors-good-practices-and-lessons-learned.

[2] X. (Frank) Chen, T. Chen, C.M. Parish, T. Graening, M.A. Sokolov, K.J. Leonard, Post-Irradiation Examination of High Fluence Baffle-Former Bolts Retrieved from a Westinghouse Two-Loop Downflow Type PWR, ORNL/TM-2019/1251, United States, 2019. https://doi.org/10.2172/1557483.

[3] X. (Frank) Chen, M.A. Sokolov, Fracture Toughness and Fatigue Crack Growth Rate Testing of Baffle-Former Bolts Harvested from a Westinghouse Two-Loop Downflow Type PWR, ORNL/TM-2021/2264, 2021.

[4] H.T. Tang, Materials Reliability Program Hot Cell Testing of Baffle/Former Bolts Removed from Two Lead PWR Plants (MRP-51), report number 1003069, EPRI technical report, 2001.

[5] X. (Frank) Chen, K.J. Leonard, M.A. Sokolov, M.A. Burke, M.N. Gussev, S.R. Clark, Specimen Fabrication from Two High Fluence Ginna Baffle Bolts, ORNL/TM-2017/455, 2017.

[6] O.K. Chopra, A.S. Rao, Degradation of LWR Core Internal Materials due to Neutron Irradiation, 2010.

[7] H.T. Tang, Materials Reliability Program Determination of Operating Parameters of Extracted Bolts (MRP-52), report number 1003076, EPRI technical report, 2001.

[8] D.J. Edwards, E.P. Simonen, F.A. Garner, L.R. Greenwood, B.M. Oliver, S.M. Bruemmer, Influence of irradiation temperature and dose gradients on the microstructural evolution in neutron-irradiated 316SS, J. Nucl. Mater. 317 (2003) 32–45. https://doi.org/https://doi.org/10.1016/S0022-3115(03)00003-5.

[9] K.J. Leonard, M.A. Sokolov, M.N. Gussev, Post-Service Examination of PWR Baffle Bolts, Part I. Examination and Test Plan, Oak Ridge National Laboratory Report, ORNL/LTR-2015/193, 2015.

[10] C.M. Parish, Chapter 5 - Multivariate Statistics Applications in Scanning Transmission Electron Microscopy X-Ray Spectrum Imaging, in: P.W.B.T.-A. in I. and E.P. Hawkes (Ed.), Adv. Imaging Electron Phys., Elsevier, 2011: pp. 249–295. https://doi.org/https://doi.org/10.1016/B978-0-12-385983-9.00005-3.

[11] A. Devaraj, D.E. Perea, J. Liu, L.M. Gordon, T.J. Prosa, P. Parikh, D.R. Diercks, S. Meher, R.P. Kolli, Y.S. Meng, S. Thevuthasan, Three-dimensional nanoscale characterisation of materials by atom probe tomography, Int. Mater. Rev. 63 (2018) 68–101. https://doi.org/10.1080/09506608.2016.1270728.

[12] A. Devaraj, T.C. Kaspar, S. Ramanan, S. Walvekar, M.E. Bowden, V. Shutthanandan, R.J. Kurtz, Nanoscale phase separation in epitaxial Cr-Mo and Cr-V alloy thin films studied using atom probe tomography: Comparison of experiments and simulation, J. Appl. Phys. 116 (2014) 193512. https://doi.org/10.1063/1.4901465.

[13] J. Zhou, J. Odqvist, M. Thuvander, P. Hedström, Quantitative Evaluation of Spinodal Decomposition in Fe-Cr by Atom Probe Tomography and Radial Distribution Function Analysis, Microsc. Microanal. 19 (2013) 665–675. https://doi.org/DOI: 10.1017/S1431927613000470.

[14] O.C. Hellman, J.A. Vandenbroucke, J. Rüsing, D. Isheim, D.N. Seidman, Analysis of Three-dimensional Atom-probe Data by the Proximity Histogram, Microsc. Microanal. 6 (2000) 437–444. https://doi.org/DOI: 10.1007/S100050010051.

[15] T.G. Lach, D.A. Collins, T.S. Byun, Evolution of the role of molybdenum in duplex stainless steels during thermal aging: From enhancing spinodal decomposition to forming heterogeneous precipitates, J. Nucl. Mater. 557 (2021) 153268. https://doi.org/https://doi.org/10.1016/j.jnucmat.2021.153268.

[16] T.G. Lach, W.E. Frazier, J. Wang, A. Devaraj, T.S. Byun, Precipitation-site competition in duplex stainless steels: Cu clusters vs spinodal decomposition interfaces as nucleation sites during thermal aging, Acta Mater. 196 (2020) 456–469. https://doi.org/https://doi.org/10.1016/j.actamat.2020.05.017.

[17] R. Hu, G.D.W. Smith, E.A. Marquis, Effect of grain boundary orientation on radiation-induced segregation in a Fe–15.2at.% Cr alloy, Acta Mater. 61 (2013) 3490–3498. https://doi.org/https://doi.org/10.1016/j.actamat.2013.02.043.

[18] T.G. Lach, A. Devaraj, K.J. Leonard, T.S. Byun, Co-dependent microstructural evolution pathways in metastable δ-ferrite in cast austenitic stainless steels during thermal aging, J. Nucl. Mater. 510 (2018). https://doi.org/10.1016/j.jnucmat.2018.08.038.

[19] W.-Y. Chen, M. Li, M.A. Kirk, P.M. Baldo, T. Lian, Effect of heavy ion irradiation on microstructural evolution in CF8 cast austenitic stainless steel, J. Nucl. Mater. 471 (2016) 184–192. https://doi.org/https://doi.org/10.1016/j.jnucmat.2015.08.032.

[20] F.A. Garner, 3.02 - Radiation-Induced Damage in Austenitic Structural Steels Used in Nuclear Reactors☆, in: R.J.M. Konings, R.E.B.T.-C.N.M. (Second E. Stoller (Eds.), Elsevier, Oxford, 2020: pp. 57–168. https://doi.org/https://doi.org/10.1016/B978-0-12-803581-8.12067-3.

[21] Y. Huang, J.M.K. Wiezorek, F.A. Garner, P.D. Freyer, T. Okita, M. Sagisaka, Y. Isobe, T.R. Allen, Microstructural characterization and density change of 304 stainless steel reflector blocks after long-term irradiation in EBR-II, J. Nucl. Mater. 465 (2015) 516–530. https://doi.org/https://doi.org/10.1016/j.jnucmat.2015.06.031.

[22] L.N. Clowers, Z. Jiao, G.S. Was, Synergies between H, He and radiation damage in dual and triple ion irradiation of candidate fusion blanket materials, J. Nucl. Mater. 565 (2022) 153722. https://doi.org/https://doi.org/10.1016/j.jnucmat.2022.153722.

[23] M. Song, K.G. Field, R.M. Cox, G.S. Was, Microstructural characterization of cold-worked 316 stainless steel flux thimble tubes irradiated up to 100 dpa in a commercial Pressurized Water Reactor, J. Nucl. Mater. 541 (2020) 152400. https://doi.org/https://doi.org/10.1016/j.jnucmat.2020.152400.

[24] C.M. Barr, P.J. Felfer, J.I. Cole, M.L. Taheri, Observation of oscillatory radiation induced segregation profiles at grain boundaries in neutron irradiated 316 stainless steel using atom probe tomography, J. Nucl. Mater. 504 (2018) 181–190. https://doi.org/https://doi.org/10.1016/j.jnucmat.2018.01.053.

[25] T.G. Lach, M.J. Olszta, S.D. Taylor, K.H. Yano, D.J. Edwards, T.S. Byun, P.H. Chou, D.K. Schreiber, Correlative STEM-APT characterization of radiation-induced segregation and precipitation of in-service BWR 304 stainless steel, J. Nucl. Mater. 549 (2021) 152894. https://doi.org/https://doi.org/10.1016/j.jnucmat.2021.152894.

[26] S.W. Chee, B. Stumphy, N.Q. Vo, R.S. Averback, P. Bellon, Dynamic self-organization in Cu alloys under ion irradiation, Acta Mater. 58 (2010) 4088–4099. https://doi.org/https://doi.org/10.1016/j.actamat.2010.03.039.

[27] R.A. Enrique, P. Bellon, Compositional Patterning in Systems Driven by Competing Dynamics Of Different Length Scale, Phys. Rev. Lett. 84 (2000) 2885–2888. https://doi.org/10.1103/PhysRevLett.84.2885.

[28] N. Almirall, P.B. Wells, S. Pal, P.D. Edmondson, T. Yamamoto, K. Murakami, G.R. Odette, The mechanistic implications of the high temperature, long time thermal stability of nanoscale Mn-Ni-Si precipitates in irradiated reactor pressure vessel steels, Scr. Mater. 181 (2020) 134–139. https://doi.org/https://doi.org/10.1016/j.scriptamat.2020.02.027.

[29] M. Mamivand, P. Wells, H. Ke, S. Shu, G.R. Odette, D. Morgan, CuMnNiSi precipitate evolution in irradiated reactor pressure vessel steels: Integrated Cluster Dynamics and experiments, Acta Mater. 180 (2019) 199–217. https://doi.org/https://doi.org/10.1016/j.actamat.2019.09.016.